Journal of Solid Mechanics and Materials Engineering

Vol. 2, No. 1, 2008

Numerical Simulation of Temperature Uniformity within Solid Particles in Cold Spray*

Hiroshi KATANODA**

** Department of Mechanical Engineering, Kagoshima University
1-21-40 Korimoto, Kagoshima, 890-0065 Japan
E-mail:katanoda@mech.kagoshima-u.ac.jp

Abstract

In the numerical simulation of temperature of particles traveling in the jet flow of cold spray, the particle temperature is usually assumed uniform. This assumption is valid for spray materials with larger thermal conductivity. For spray materials with smaller thermal conductivity, however, this assumption may not be valid. This paper numerically clarifies the spray conditions for which the assumption of the temperature uniformity of the particle is no longer valid in the cold spray.

Key words: Cold Spray, Numerical Simulation, Spray Particle, Temperature Uniformity, Thermal Conductivity

1. Introduction

In many engineering fields, thermal spraying is commonly applied to mechanical parts to enhance surface properties of solid surfaces. In conventional thermal spray methods, such as plasma spray or high velocity oxy-fuel (HVOF) thermal spray, powder is injected into a flow of hot process-gas which has a temperature much higher than the material's melting point. Then, the particles are accelerated and heated while traveling in the downstream direction, and finally, they contact the solid substrate to form a coating. Due to the high gas-temperature, the spray particles are fully or partially melted when they hit the substrate, resulting in degradation of the performance of the coating.

An innovative coating process, called cold spray, was invented in the 1980's in Russia, then a U.S. patent was issued in 1994 [1]. The schematic diagram of the cold spray is shown in Fig.1. The cold spray uses electrically heated low-temperature and high-pressure gas; the ranges of the temperature and pressure upstream of the nozzle are normally 400 – 1100 K and 1 – 4 MPa, respectively. The gas selected is normally nitrogen or helium. Due to the low temperature of the process gas compared to the conventional thermal spray methods, even the temperature-sensitive material, such as copper [2, 3] or titanium [4], can be coated

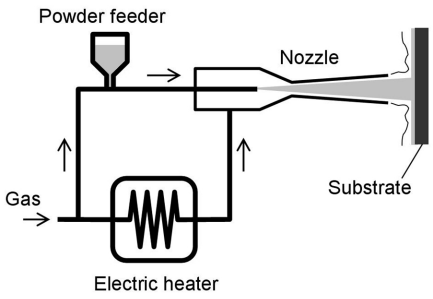

Fig. 1 Schematic diagram of cold spray.

*Received 22 Aug., 2007 (No. 07-0379)
[DOI: 10.1299/jmmp.2.58]

by the cold spray without thermal degradation of the feed stock powder.

Experimentally it is well known that the particles start to deposit on the substrate when the impact velocity exceeds material-dependent threshold value, which is called 'critical velocity'. The larger the particle temperature at impact, the smaller the critical velocity becomes [5]. It means that the information of the particle impact velocity and temperature are of importance from the view point of the deposition efficiency. In addition, it is also well known that mechanical properties of the coating are strongly dependent on the velocity and temperature of the particles at impact. Therefore, knowing the particle velocity and temperature at impact is critically important to optimize the cold spray process. The measurement of the particle velocity is conducted by visualizing the particle using a laser light sheet [6, 7] or laser two-focus velocimeter [8]. As for the particle temperature, it can be measured by the two-color pyrometer if the particle temperature, that is thermal radiation from the particle, is high enough to be detected, as in the plasma spray or HVOF thermal spray [9]. In the cold spray, however, thermal radiation from the particle is too small to be detected by using the two-color pyrometer. As far as the author knows, there is no published report on the measurement of the particle temperature of the cold spray.

The alternative way of obtaining the information of the velocity and temperature of the particle is the numerical simulation, which is the author's area of study. When computing the particle temperature in the cold spray, the temperature within the particle is usually assumed to be uniform [2, 10, 11]. Likewise, when performing the computation of solid deformation of the particle by the finite element method [12, 13], the initial particle-temperature can be assumed to be uniform. The assumption of the uniform temperature is considered to be valid if the selected material is pure metals or alloys, which has been used in the experiment of cold spray. This is because the Biot number for the pure metals or alloys in the cold spray is well below 0.1 [2], which allows the assumption of the uniform temperature. As for recently cold-sprayed materials such as WC-Co [14], CoNiCrAlY [15] and Al_2O_3 [16] have been used however, their thermal conductivity is in the order of one-tenth or smaller than that for pure metals, such as copper. This means that the temperature distribution in the particle may need to be considered. However, there seems to be no research work of the numerical simulation about the temperature distribution within the particle in the cold spray.

The objective of the present paper is to numerically clarify the spray conditions for which the assumption of the temperature uniformity of the particle is no longer valid. The effects of the gas type, gas temperature, material type of the particle, and particle diameter on the temperature uniformity are investigated by the numerical simulation.

2. Numerical Method

2.1 Gas flow

The assumptions used in the present computational fluid dynamics (CFD) model are listed as follows:

1) The gas flow is two-dimensional axisymmetric.
2) The gas is thermally and calorically perfect.
3) The gas species inside and outside the nozzle are the same.
4) The momentum transfer and heat transfer from the particle to the gas flow are neglected.

The above assumptions are normally used in the CFD model of the cold spray. The governing equations of the gas flow are given by the two-dimensional axisymmetric, time-dependent Navier-Stokes equations along with the k-ε turbulence model [17]. The governing equations are solved sequentially in an implicit, iterative manner using a finite difference formulation. The governing equations are solved with the third-order, upwind,

total variation diminishing scheme. The helium and nitrogen were used as a process gas independently in the CFD model. The values of stagnation pressure p_{os} and temperature T_{os} upstream of the nozzle are summarized in Table 1. The thermal conductivity of He gas is about 5 – 6 times as much as that of N_2 gas in the range of 300 – 1200 K. It means that the temperature non-uniformity of the particle is expected to be more serious for He as a process gas than N_2, as can be understood from Eq.(15) which is introduced later in section 3.1. In this paper, therefore, more discussion is made for Cases 1 and 2.

Figure 2 shows a nozzle used in the CFD model. The distance from the nozzle exit to the substrate is set at 20 mm. The size of the computational grid used in this simulation is 200×45 grids inside the nozzle, and 100×145 grids outside the nozzle. This grid size was found to be enough to obtain an almost grid-size-independent solution; the coarse computational grids, 140×30 and 66×96 for inside and outside the nozzle, respectively, showed negligible change in the gas velocity along the center line.

The steady one-dimensional isentropic theory [18] calculates the Mach number of the gas flow at the nozzle exit, the design Mach number M_d, of 4.84 for He. According to the theory of gasdynamics, the nozzle of M_d = 4.86 generates an over-expanded flow at p_{os} = 2 MPa of He gas. In this case, we expect that the flow separates from the inner nozzle-wall by shock-wave/boundary-layer interaction [19]. The similar flow pattern is also expected for the N_2 cases.

Table 1 Gas conditions.

	Gas	p_{os}	T_{os}
Case 1	Helium	2 MPa	900 K
Case 2	Helium	2 MPa	1200 K
Case 3	Nitrogen	2 MPa	900 K
Case 4	Nitrogen	2 MPa	1200 K

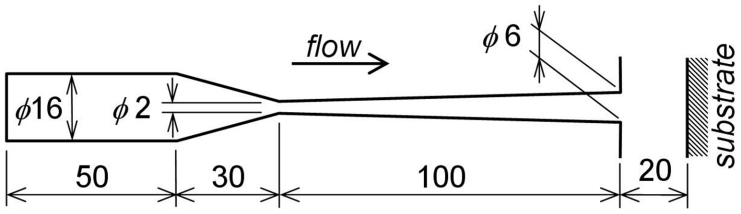

Fig. 2 Nozzle geometry.

2.2 Particle behavior

The following assumptions are used to simulate the particle velocity and temperature to simplify the computation.

1) The particles are isometric in shape, including sphere.
2) The particles travel along the center line.
3) The interaction between the particles is negligible.
4) The particle is accelerated only by gasdynamic drag force.
5) The particle is heated by the gas flow through heat transfer.
6) The temperature distribution within the particle is spherically symmetric.
7) The material properties of the particle are constant.

Then, the equation of particle motion is written as;

$$m_p u_p \frac{du_p}{dx} = \frac{1}{2} c_d \rho_g \left(u_g - u_p\right) \cdot \left|u_g - u_p\right| A_p \tag{1}$$

where x is the axial distance along the center line from the nozzle throat, ρ_g the gas density, u_g the gas velocity, m_p the mass of the particle, u_p the particle velocity, A_p the projected area of the particle, c_d the drag coefficient of the particle, respectively. For the spherical particle, c_d was calculated by using a database made from the experimental data [20], along with a correction given by Eq.(2) due to high temperature of the gas [21].

$$c_d = c_{d,\exp} f_{prop}^{-0.45} \tag{2}$$

where $c_{d,exp}$ is the drag coefficient obtained from the database. The correction factor f_{prop} is given by Eq.(14) later in this section. The value of $c_{d,exp}$ in Eq.(2) is obtained by the particle Mach number M_p, defined by the following equation, and the particle Reynolds number R_{ep}, defined by Eq.(12) later in this section.

$$M_p = \left|u_g - u_p\right| / a_g \tag{3}$$

where a_g is the sound speed of the gas.

To take into consideration the fact that powders used in the cold spray process are not always spherical, a formula for the drag coefficient, which accounts for particle non-spherical shape using so-called sphericity [22] ϕ is used in this paper. The sphericity is defined as the ratio of the surface area of a sphere with equivalent volume to the actual surface area of the particle. For non-spherical particle, the drag coefficient c_d in Eq.(2) is replaced by c_d / K_2. Then, $c_{d,exp}$ in Eq.(2) is obtained by M_p and $K_1 K_2 R_{ep}$, instead of R_{ep}, where K_1 and K_2 are the Stokes' shape factor and the Newton's shape factor, respectively, which can be determined by the following equations for the isometric particles [22].

$$K_1^{-1} = \frac{1}{3} + \frac{2}{3\sqrt{\phi}} \tag{4}$$

$$\log\left(K_2\right) = 1.8148\left(-\log\phi\right)^{0.5743} \tag{5}$$

The spherically symmetric temperature distribution within a particle can be calculated by the following equation of heat conduction;

$$\rho_p C \frac{\partial T_p}{\partial t} = \frac{1}{r^2} \frac{\partial}{\partial r} \left(r^2 k_p \frac{\partial T_p}{\partial r} \right) \tag{6}$$

where T_p is the particle temperature, ρ_p the particle density, C the specific heat of the particle, k_p the thermal conductivity of the particle, t the time, r the radial distance measured from the center of the particle. The boundary conditions at the outer surface and center of the particle are given as;

$$k_p \left. \frac{\partial T_p}{\partial r} \right|_{r=d_p/2} = \alpha \left(T_g - T_{p,w}\right) \tag{7}$$

$$\left. \frac{\partial T_p}{\partial r} \right|_{r=0} = 0 \tag{8}$$

where T_g is the gas temperature, $T_{p,w}$ the particle temperature at its surface, d_p is either the particle diameter if the particle is spherical or the equivalent diameter if not. The subscript w in Eq.(7) indicates the surface of the particle. The heat transfer coefficient α in Eq.(7) is given as;

$$\alpha = k_{g,f} N_u / d_p \tag{9}$$

Here, N_u is the Nusselt number, k_g the thermal conductivity of the gas. The subscript f in Eq.(9) means the value at the film temperature, T_f, defined as;

$$T_f = (T_g + T_p)/2 \tag{10}$$

The Nusselt number, N_u, in Eq.(9) was computed by Ranz-Marshall correlation along with the correction factors [21].

$$N_u = \left(2 + 0.6R_{ep}^{1/2}P_r^{1/3}\right)\cdot\left(c_p / c_{p,w}\right)^{0.38} f_{prop}^{0.6} \tag{11}$$

where c_p is the specific heat of the gas at constant pressure. The particle Reynolds number R_{ep} and the Prandtl number of the gas P_r in Eq.(11) are defined as;

$$R_{ep} \equiv \rho_{g,f} d_p \left|u_g - u_p\right| / \mu_{g,f} \tag{12}$$

$$P_r \equiv \mu_{g,f} c_{p,f} / k_{g,f} \tag{13}$$

where μ_g is the gas viscosity. The factor f_{prop} in Eq.(11) represents the effect of the gas temperature in the boundary layer on the particle surface, and is given as follows [21];

$$f_{prop} = \frac{\rho_g \mu_g}{\rho_{g,w} \mu_{g,w}} \tag{14}$$

The particle velocity and temperature were determined from a step-wise integration of Eqs. (1) and (6), respectively. To solve the right-hand side of Eq.(6) numerically, equally spaced 30 grids were applied along the radius of the particle from the center to the surface.

The powder-materials selected are WC-12Co, Ti, Ti6Al4V and Al_2O_3 covering large to small material density, specific heat, and thermal conductivity, as shown in Table 2. The range of the particle diameter is 5 – 150 μm for each material, and the sphericity is set at 1.0 for the material conditions shown in Table 2. The particles are injected in the gas flow at 20 mm upstream of the throat on the center line.

Table 2 Material conditions.

Material	Density [kg/m^3]	Specific heat [J/(kg·K)]	Thermal conductivity [W/(m·K)]
WC-12Co	14320	295	49
Ti	4510	528	22
Ti6Al4V	4420	537	7.6
Al_2O_3	3900	1424	6.3

3. Results and discussion

3.1 Validation of simulation code

To validate the numerical model used in this study, the accuracy of the calculated particle velocity and temperature are investigated in this section. Firstly, as for the particle velocity, the experiment conducted by Jodoin, et al. [6] was selected as the test case. In their experiment, the compressed nitrogen, as well as helium, of 2.0, 2.4 MPa and 573 – 773 K were both used as the process gases. The gases were discharged into the atmosphere through a converging-diverging nozzle, which had a throat diameter of 2.6 mm, an exit diameter of 8.4 mm, and a conically diverging length of 65 mm. The particle used in their experiment was the water-atomized pure nickel with a mean diameter of 19 μm. The measurement of the particle velocity was conducted by using a fast-shutter CCD camera along with a laser sheet to illuminate the particles traveling in the jet flow without the substrate. The measured

particle velocities were averaged over the distance of 16 mm from the nozzle exit. In this paper, nitrogen gas of 2.0 MPa and 573 – 773 K were selected for the code validation. The comparison between the measured and calculated particle velocities are shown in Fig.3. In the numerical simulation, the particle diameter and the sphericity were set at 19 μm and 0.9, respectively. The simulated particle velocities were averaged over 16 mm from the nozzle exit. Figure 3 shows that the particle velocities obtained by the numerical simulation agree well with the experimental results.

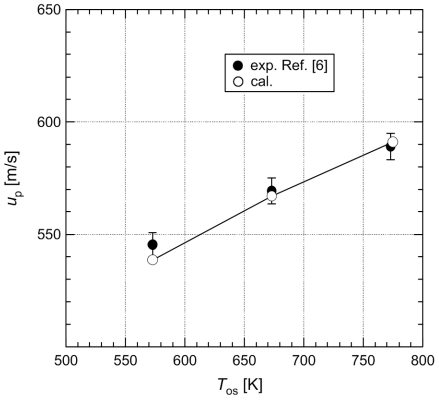

Fig. 3 Comparison of particle velocities of Ni.

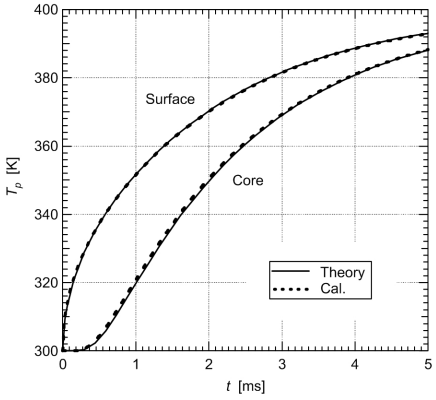

Fig. 4 Comparison of particle temperatures.

Secondly, the validity of the calculation of the particle temperature is examined by comparing it with the theoretical solution because no experimental data of the particle temperature is available in the cold spray. The powder material selected for this validation is the spherical polypropylene resin, which has a material density of 850 kg/m^3, specific heat of 2.1 kJ/(kg·K), and thermal conductivity of 0.19 W/(m·K). The diameter of the particle is set at 50 μm, and its initial temperature is set at 300 K. In the calculation, the particle is immersed into a stationary hydrogen gas of 0.1 MPa and 400 K. For these conditions, the Biot number Bi for the spherical particle given by Eq.(15) [23] is calculated as 0.396.

$$Bi = \frac{N_u}{6} \cdot \frac{k_g}{k_p} \tag{15}$$

Generally, the particle temperature can not be regarded uniform when $Bi > 0.1$. Therefore, under the conditions mentioned above the temperature within the particle is expected to be non-uniform. The time histories of the particle temperature at its surface and central core are shown in Fig.4. The vertical axis shows the particle temperature, and the horizontal axis shows the time measured from the moment when the particle is immersed in the hydrogen gas. The solid lines show the theoretical solutions obtained by mathematically solving Eq.(6). The dotted lines show the results obtained by numerically integrating Eq.(6). Figure 4 shows that the numerical results almost exactly agree with that of mathematical solutions, demonstrating the validity of the present method of calculating the particle temperature.

3.2 Gas/particle flow

The simulated Mach number contour is shown in Fig.5 for Case 1. The axial distance measured from the throat, x, is shown in the bottom side of the figure. The substrate is located at x = 120 mm. Figure 5 shows that the gas flow is accelerated to supersonic flow through the throat in the downstream direction. Then, the Mach number reaches the maximum value of M_g = 2.91 at x ~ 42 mm, around where the flow separates from the nozzle-wall as was theoretically predicted in the previous chapter.

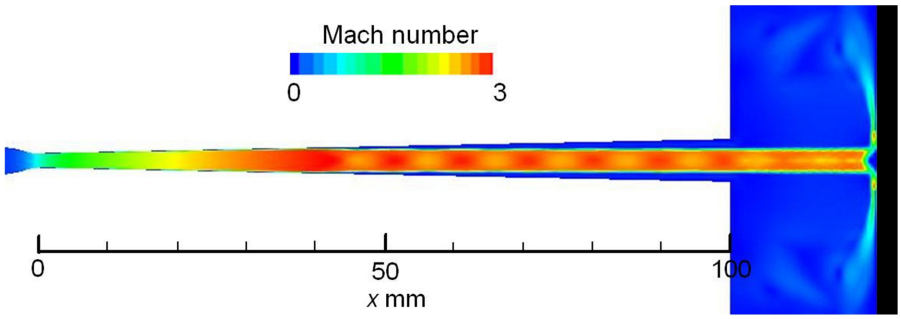

Fig. 5 Mach number contour for Case 1.

Figure 6(a) shows the temperatures of the He gas, T_g, and 60 μm-Al_2O_3 particle, T_p, along the center line for Case 1. The gas temperature suddenly decreases from the stagnant value by passing through the throat, until the flow reaches the separation point $x \sim 42$ mm. Then, the gas temperature starts fluctuating in the downstream direction due to the compression/expansion waves in the shock-train [24, 25] generated in the nozzle. After exiting the nozzle the gas temperature sharply rises at $x = 118.5$ mm to reach almost stagnant value on the substrate after going through the normal shock wave (NSW). As for the particle, the surface temperature increases faster than the core temperature while traveling in the hotter subsonic flow in the upstream part of the throat. After the throat, the surface and core temperatures start decreasing because the gas temperature is below the surface temperature. Due to the small value of thermal conductivity of Al_2O_3, there exists 20 – 30 K temperature difference between the particle surface and core during the downstream process from $x \sim 30$ mm to the substrate.

The radial temperature-distributions of 60 μm-Al_2O_3 at three axial locations of $x = 0$ (at throat), 50, 120 mm (on substrate) are shown in Fig.6(b) for Case 1. The horizontal axis shows the radial distance from the core divided by the particle diameter, r/d_p. At $x = 0$ mm, the particle temperature gradually increases in the radial direction due to the heating by the hotter subsonic gas flow. At $x = 50$ mm in the nozzle, however, the particle temperature gradually decreases in the radial direction due to the cooling by the colder supersonic gas flow. At $x = 120$ mm, on the substrate, the particle temperature close to the surface increases due to the heating by the stagnant hotter gas, as can be seen in Fig.6(a). At the moment it is

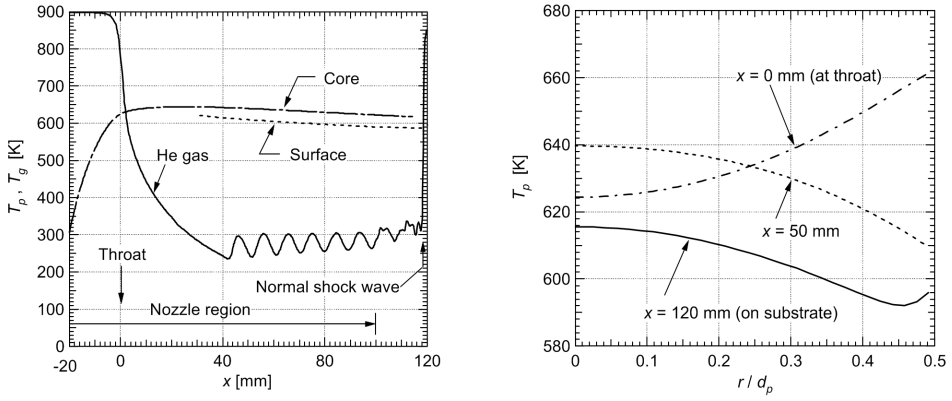

(a) Gas/particle temperature along center line (b) Radial temperature-distribution of particle

Fig.6 Numerical results for Case 1 (60 μm Al_2O_3).

unclear in the experiment of the cold spray [16] whether the Al_2O_3 particle can be deposited on the first Al_2O_3 layer which has contacted the substrate. However, the information as shown in Fig.6 help us deeply understand the physics of the cold spray process.

The maximum temperature-differenc in the particle, $\Delta T_{p,\max}$, defined by the following equation is shown in Fig.7(a) for Case 1 with Al_2O_3 particle.

$$\Delta T_{p,\max} = T_{p,\max} - T_{p,\min} \tag{16}$$

where $T_{p,\max}$ and $T_{p,\min}$ are the maximum and minimum temperature in the particle, respectively, at arbitrary axial location x. The value of $\Delta T_{p,\max}$ does not always equal to the difference between the surface and core temperatures of the particle, as can be seen in Fig.6(b). In Fig.7(a), $\Delta T_{p,\max}$ for d_p = 5 μm is less than 14 K in the nozzle. The local minimum of $\Delta T_{p,\max}$ for d_p = 60 μm at x = 10 mm corresponds to the location where the surface temperature decreases across the core temperature, as was indicated in Fig.6(a). After taking the local minimum value, $\Delta T_{p,\max}$ for d_p = 60 μm increases in the downstream direction to reach the maximum value of about 33 K at x ~ 90 mm, then the value gradually decrease towards the substrate. For d_p = 150 μm, $\Delta T_{p,\max}$ sharply increases until the throat, then, it decreases towards the nozzle exit. This trend is due to the heating of the particle surface in the hotter subsonic gas flow, and cooling of the particle surface in the colder supersonic gas flow, with lower core temperature than the surface temperature all through the trajectory in the nozzle.

Figure 7(b) shows the enlargement of Fig.7(a) from 10 mm downstream of the nozzle exit to the substrate, 110 mm < x < 120 mm, to clearly show the effect of the NSW on the non-uniformity of the particle temperature. For d_p = 5 μm, $\Delta T_{p,\max}$ sharply rises after the NSW from 0 K to 32 K due to the heating by the stagnant gas. For d_p = 60 μm, $\Delta T_{p,\max}$ decreases after going through the NSW because only the outer region of the particle is heated by the stagnant gas, resulting in the decrease in $\Delta T_{p,\max}$, as was seen in Fig.6(b). On the other hand, $\Delta T_{p,\max}$ increases between the NSW and the substrate for d_p = 150 μm. This increase occurs because the core temperature is below the outer temperature of the particle all through the trajectory of the particle.

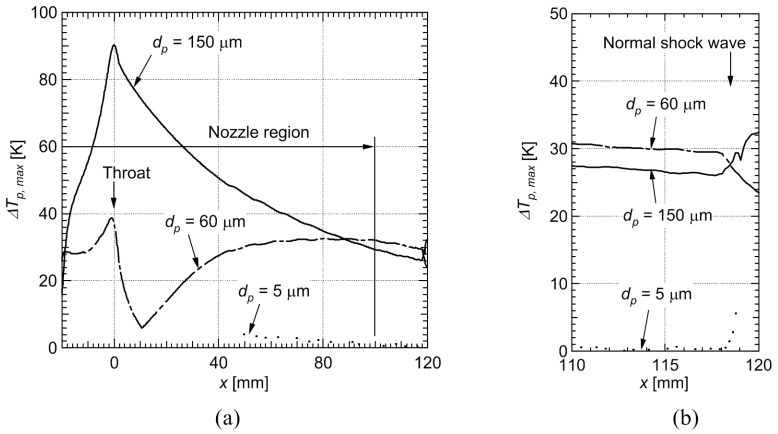

Fig. 7 Maximum temperature-difference in particle for Case 1 (Al_2O_3).

The temperature distribution in the particle at impact on the substrate is much more valuable than that in the jet flow when considering the quality of the coating. The maximum temperature-difference in the particle at impact, $\Delta T_{pi,\max}$, divided by the core temperature at impact, $T_{pi,\text{core}}$, is shown in Fig.8(a) – (d) for Cases 1 – 4, respectively, as a function of particle diameter. The value of $\Delta T_{pi,\max}$ included in the vertical axis is defined as;

$$\Delta T_{pi,\max} = T_{pi,\max} - T_{pi,\min} \tag{17}$$

where the subscript i shows the impact condition. Figure 8(a) for Case 1 shows that $\Delta T_{pi,\max}/T_{pi,\text{core}}$ is less than 3.3 % for materials of $k_p > 20$ W/(m·K), WC-12Co and Ti, for 5 μm ≤ d_p ≤ 150 μm. As for Al_2O_3, k_p = 6.3 W/(m·K), there are three local peaks of $\Delta T_{pi,\max}/T_{pi,\text{core}}$ for 5 μm ≤ d_p ≤ 150 μm. The first peak occurs at d_p = 5 μm, due to the heating of particle with a smaller heat capacity by the stagnant gas between the NSW and the substrate, as was seen in Fig.7. Then, the second peak takes place at d_p = 60 μm, due to the higher core temperature in the colder supersonic gas flow, as was seen in Fig.6(b). And then, the third peak occurs at d_p = 150 μm, due to the lower core temperature of the particle with a larger heat capacity. Although it is unclear at the moment that above what percent of $\Delta T_{pi,\max}/T_{pi,core}$ is significant to the coating quality or deposition efficiency, the author pays special attention to $\Delta T_{pi,\max}/T_{pi,core} \geq 5$ %, which covers roughly larger values of $\Delta T_{pi,\max}/T_{pi,core}$ in Fig.8(a) – (d). From Fig.8(a), the value of $\Delta T_{pi,\max}/T_{pi,core}$ exceeds 5 % for Al_2O_3 (d_p ≤ 5 μm and d_p ≥ 140 μm) and Ti6Al4V (d_p ≤ 10 μm).

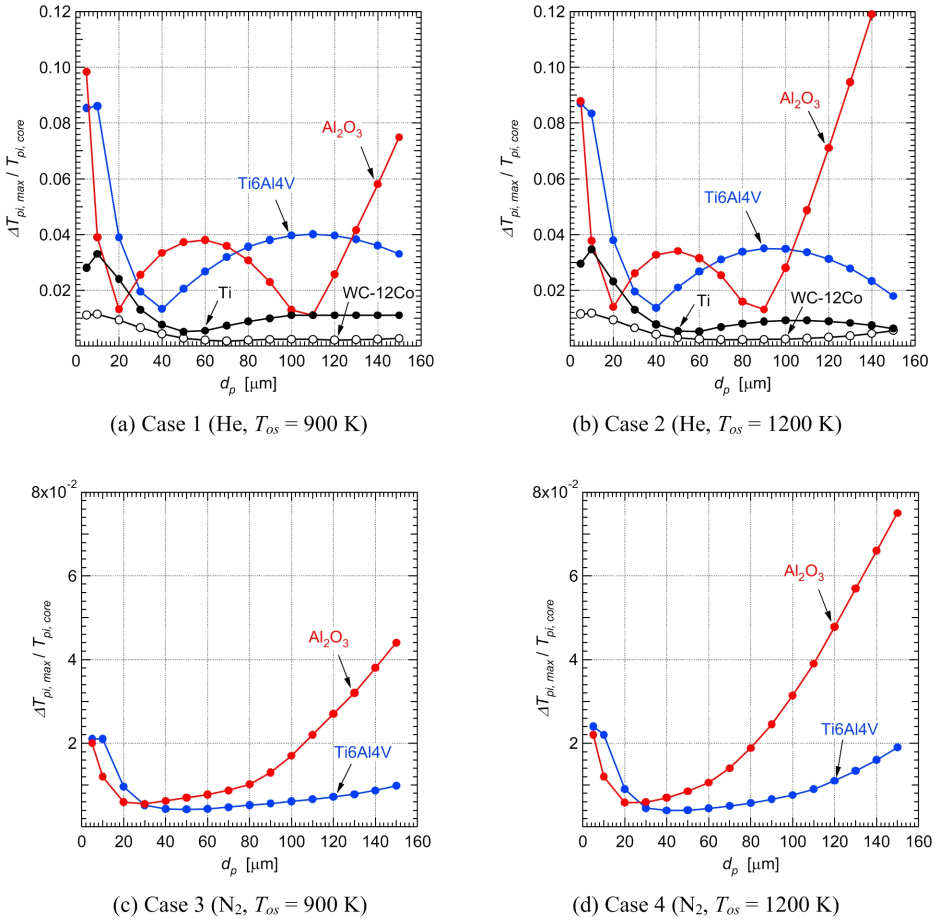

(a) Case 1 (He, T_{os} = 900 K)

(b) Case 2 (He, T_{os} = 1200 K)

(c) Case 3 (N_2, T_{os} = 900 K)

(d) Case 4 (N_2, T_{os} = 1200 K)

Fig. 8 Maximum temperature-difference against core temperature at impact on substrate.

Figure 8(b) shows $\Delta T_{pi,\max}/T_{pi,\text{core}}$ for Case 2, a higher gas-temperature case of He. The values of $\Delta T_{pi,\max}/T_{pi,\text{core}}$ for WC-12Co and Ti are less than 3.5 %. The most important feature in Fig.8(b) compared to Fig.8(a) is that the third local peak of $\Delta T_{pi,\max}/T_{pi,\text{core}}$ for Al_2O_3 is highly elevated, where $\Delta T_{pi,\max}/T_{pi,\text{core}}$ increases almost linearly from 1.3 % at d_p = 90 μm to 14.4 % at d_p = 150 μm ($\Delta T_{pi,\max}/T_{pi,\text{core}}$ for d_p = 150 μm is not shown in Fig.8(b)). The value of $\Delta T_{pi,\max}/T_{pi,core}$ exceeds 5 % for Al_2O_3 (d_p ≤ 5 μm and d_p ≥ 110 μm) and

Ti6Al4V ($d_p \leq 10$ μm) in Fig.8(b).

Figure 8(c) and (d) shows $\Delta T_{pi,\max}/T_{pi,\text{core}}$ for Cases 3 and 4, respectively. The values of $\Delta T_{pi,\max}/T_{pi,\text{core}}$ of Ti and WC-12Co were found less than 1 % in the range of 5 μm $\leq d_p \leq$ 150 μm for Cases 3 and 4. Therefore, calculated data of Ti and WC-12Co are not plotted in Fig.8(c) and (d). From the figures, $\Delta T_{pi,\max}/T_{pi,\text{core}}$ exceeds 5 % only for Al_2O_3 of $d_p > \sim 120$ μm sprayed by the N_2 gas at $T_{0s} = 1200$ K.

Finally, radial temperature distributions of Al_2O_3 and Ti6Al4V particles on the substrate are shown in Fig.9(a) and (b) for Cases 1 and 2, respectively. The solid curves are for Al_2O_3 and the dotted curves are for Ti6Al4V. The particle diameter selected in the figure are those for the local maximum values of $\Delta T_{pi,\max}/T_{pi,\text{core}}$ in Fig.8(a) and (b). The vertical axis of Fig.9(a) shows the particle temperature at arbitrary radial location at impact T_{pi}, divided by that at the core at impact $T_{pi,core}$. The horizontal axis shows the radial distance r divided by the particle diameter. Figure 9(a) shows that the smallest particles of 5 μm-Al_2O_3 and 5 μm-Ti6Al4V have higher temperatures at the surface by 9 – 10 %, compared to those at the core. This non-uniformity of temperature is caused by the high-temperature, stagnant gas between the NSW and the substrate. Although the particle is heated in a short distance of 1.5 mm between the NSW and the substrate, the heat energy of higher gas-temperature penetrates well inside the particle due to smaller heat capacity. On the other hand, the larger particles of 60 μm-Al_2O_3 and 110 μm-Ti6Al4V have lower temperatures close the surface by 4 %, compared to the core temperatures. This is because the heat energy of a higher gas-temperature can only raise the particle surface temperature due to larger heat capacity. For 150 μm-Al_2O_3, the core temperature is lower than the surface temperature by 8 % because the central part of the particle is not well affected by the gas flow through the nozzle due to the large heat capacity, as was explained in Fig.7(a).

Figure 9(b) shows $T_{pi}/T_{pi,\text{core}}$ for Case 2, a higher gas-temperature case. The distributions of $T_{pi}/T_{pi,\text{core}}$ in Fig.9(b) is almost the same as those in Fig.9(a), except that the $\Delta T_{pi,\max}/T_{pi,\text{core}}$ for 150 μm-Al_2O_3 particle increases from 8 % in Fig.9(a) to 15 % in Fig.9(b). This increase is caused by the hotter He gas in the nozzle for Case 2, especially in the subsonic region upstream of the throat, compared to Case 1. As for Case 4 (not shown in this paper), the radial distributions of $T_{pi}/T_{pi,\text{core}}$ of Al_2O_3 particles were found similar to that of Al_2O_3 particle of $d_p = 150$ μm in Fig.9(b) in the range of $d_p > \sim 120$ μm, for which $\Delta T_{pi,\max}/T_{pi,\text{core}} > 5$ % as shown in Fig.8(d).

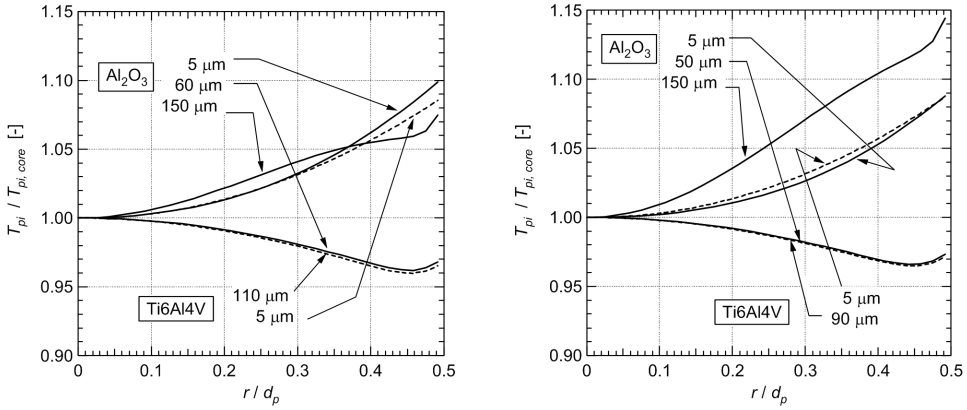

(a) Case 1 (He, T_{os} = 900 K)

(b) Case 2 (He, T_{os} = 1200 K)

Fig. 9 Radial temperature distributions of Al_2O_3 and Ti6Al4V on substrate.

4. Concluding remarks

The numerical simulation of the cold spray was performed to clarify the spray conditions that are needed to consider the radial temperature distribution of the spray particle. The He and N_2 were used as the process gas respectively. The stagnation pressure upstream of the throat was set at 2 MPa and the stagnation temperature T_{os} was set at 900 and 1200 K, respectively. The spray materials selected were WC-12Co, Ti, Ti6Al4V and Al_2O_3. The range of the particle-diameter d_p was 5 – 150 μm. Special attention was paid to the maximum temperature difference in the particle at impact, $\Delta T_{pi,\max}$, against the core temperature at impact, $T_{pi,core}$. The results are summarized as follows:

(1) If N_2 is used as a process gas, $\Delta T_{pi,\max}/T_{pi,core}$ exceeds 5 % only when Al_2O_3 particle of $d_p > \sim 120$ μm is sprayed at $T_{0s} = 1200$ K.

(2) There are three peaks of $\Delta T_{pi,\max}/T_{pi,core}$ when it is plotted against d_p for He gas. The first peak occurs at the smaller particle diameter due to the smaller heat capacity through the heating by the stagnant gas between the normal shock wave and the substrate. The second peak takes place at the medium particle diameter due to the higher core temperature in the colder supersonic gas flow. The third peak occurs at the larger particle diameter due to the lower core temperature with larger heat capacity. The first and third peaks of $\Delta T_{pi,\max}/T_{pi,core}$ are more significant than the second one.

(3) When Al_2O_3 is sprayed by He gas, $\Delta T_{pi,\max}/T_{pi,core}$ exceeds 5 % in the range of both i) $d_p \leq 5$ μm and $d_p \geq 140$ μm for $T_{os} = 900$ K, ii) $d_p \leq 5$ μm and $d_p \geq 110$ μm for $T_{os} = 1200$ K by the first and third reasons described in (2).

(4) When Ti6Al4V is sprayed by He gas, $\Delta T_{pi,\max}/T_{pi,core}$ exceeds 5 % in the range of $d_p \leq 10$ μm for $T_{os} = 900$ K and 1200 K by the first reason described in (2).

(5) Even if He is used as a process gas, $\Delta T_{pi,\max}/T_{pi,core}$ is less than 3.5 % for WC-12Co and Ti particles.

References

(1) Kosarev, V.F., at al., On some aspects of gas dynamics of the cold spray process, *Journal of Thermal Spray Technology*, Vol. 12, No. 2 (2003), pp. 265-281.

(2) Stoltenhoff, T., et al., An analysis of the cold spray process and its coatings, *Journal of Thermal Spray Technology*, Vol. 11, No. 4 (2002), pp. 542-550.

(3) Dykhuizen, R.C., et al., Impact of high velocity cold spray particles, *Journal of Thermal Spray Technology*, Vol. 8, No. 4 (1999), pp. 559-564.

(4) Sakaki, K., et al., Influence of substrate conditions and traverse speed on cold sprayed coatings, *Proceedings of International Thermal Spray Conference and Exposition* 2004, (2004-5), 5pages.

(5) Assadi, H., et al., Bonding mechanism in cold gas spraying, *Acta Materialia*, Vol. 51, No. 15 (2003), pp. 4379-4394.

(6) Jodoin, B., et al., Cold spray modeling and validation using an optical diagnostic method, *Surface & Coatings Technology*, Vol. 200, No. 14-15 (2006), pp. 4424-4432.

(7) Fukanuma, H., et al., In-flight particle velocity measurements with DPV-2000 in cold spray, *Surface & Coatings Technology*, Vol. 201, No. 5 (2006), pp. 1935-1941.

(8) Gilmore, D.L., et al., Particle velocity and deposition efficiency in the cold spray process, *Journal of Thermal Spray Technology*, Vol. 8, No. 4 (1999), pp. 576-582.

(9) Legoux J.-G., et al., Evaluation of four high velocity thermal spray guns using WC-10% Co-4%Cr cermets, *Journal of Thermal Spray Technology*, Vol. 11, No. 1 (2002), pp. 86-94.

(10) Li, W.-Y. and Li, C.-J., Optimal design of a novel cold spray gun nozzle at a limited space, *Journal of Thermal Spray Technology*, Vol. 14, No. 3 (2005), pp. 391-396.

(11) Han, T., et al., Effects of spray conditions on coating formation by the kinetic spray

process, *Journal of Thermal Spray Technology*, Vol. 14, No. 3 (2005), pp. 373-383.
(12) Schmidt, T., et al., High velocity impact phenomena and coating quality in cold spraying, *Proceedings of International Thermal Spray Conference and Exposition* 2005, 7pages.
(13) Yokoyama, K., et al., Simulation of solid particle impact behavior for spray processes, *Materials Transactions*, Vol. 47, No. 7 (2006), pp. 1697-1702.
(14) Kim, H.-J., et al., Fabrication of WC-Co coatings by cold spray deposition, *Surface & Coatings Technology*, Vol. 191, No. 2-3 (2005), pp. 335-340.
(15) Richer, P., et al., Properties of cold sprayed nickel based coatings, *Proceedings of International Thermal Spray Conference and Exposition* 2006, 6pages.
(16) Veräjänkorva, S., et al., Influence of powder type and properties on ceramic layer deposition by cold spraying, *Proceedings of International Thermal Spray Conference and Exposition* 2006, 6pages.
(17) Sarkar, S., et al., The analysis and modeling of dilatational terms in compressible turbulence, *Journal of Fluid Mechanics*, Vol. 227 (1991), pp.473-493.
(18) Zucrow, M.J. and Hoffman, J.D., *Gas dynamics*, (1976), pp. 160-181, John Wiley & Sons.
(19) Kim, H.D., Matsuo, K. and Setoguchi, T., Investigation on onset of shock-induced separation, *Shock Waves*, Vol. 6, No. 5 (1996), pp. 275-286.
(20) Bailey, A.B. and Hiatt, J., Sphere drag coefficient for a broad range of Mach and Reynolds numbers, *AIAA Journal*, Vol. 10, No. 11 (1972), pp. 1436-1440.
(21) Wan, Y.P., et al., Model and powder particle heating, melting, resolidification, and evaporation in plasma spraying processes, *Journal of Heat Transfer*, Vol. 121, No. 3 (1999), pp. 691-699.
(22) Ganser, G.H., A rational approach to drag prediction of spherical and nonspherical particles, *Powder Technology*, Vol. 77, No. 2 (1993), pp. 143-152.
(23) Li, M. and Christofides, P.D., Feedback control of hvof thermal spray process accounting for powder size distribution, *Journal of Thermal Spray Technology*, Vol. 13, No.1 (2004), pp. 108-120.
(24) Matsuo, K., et al., Shock train and pseudo-shock phenomena in internal gas flows, *Progress in Aerospace Sciences*, Vol. 35, No. 1 (1999), pp. 33-100.
(25) H. Katanoda, et al., Experimental study on shock wave structures in constant-area passage of cold spray nozzle, *Journal of Thermal Science*, Vol.16, No. 1 (2007), pp. 40-45.